Understanding summertime peroxyacetyl nitrate (PAN) formation and its relation to aerosol pollution: Insights from high-resolution measurements and modeling

Baoye Hu[1,3,4], Naihua Chen[1,6], Rui Li[7], Mingqiang Huang[1,3,4], Jinsheng Chen[2,5*], Youwei Hong[2,5], Lingling Xu[2,5], Xiaolong Fan[2,5], Mengren Li[2,5], Lei Tong[2], Qiuping Zheng[8], Yuxiang Yang[6*]

[1]College of Chemistry, Chemical Engineering and Environment, Minnan Normal University, Zhangzhou, China, 363000

[2]Center for Excellence in Regional Atmospheric Environment, Institute of Urban Environment, Chinese Academy of Sciences, Xiamen 361021, China

[3]Fujian Provincial Key Laboratory of Modern Analytical Science and Separation Technology, Minnan Normal University, Zhangzhou, China, 363000

[4]Fujian Province University Key Laboratory of Pollution Monitoring and Control, Minnan Normal University, Zhangzhou, China, 363000

[5]Fujian Key Laboratory of Atmospheric Ozone Pollution Prevention, Chinese Academy of Sciences, Xiamen 361021, China

[6]Pingtan Environmental Monitoring Center of Fujian, Pingtan 350400, China

[7]Key Laboratory of Geographic Information Science of the Ministry of Education, School of Geographic Science, East China Normal University, Shanghai 200241, PR China

[8]Xiamen Key Laboratory of Straits Meteorology, Xiamen Meteorological Bureau, Xiamen 361012, China

Correspondence to: Jinsheng Chen (jschen@iue.ac.cn) & Yuxiang Yang (907460293@qq.com)

Abstract: Peroxyacetyl nitrate (PAN), a key indicator of photochemical pollution, is generated similarly to ozone (O_3), through reactions involving specific volatile organic compounds (VOCs) and nitrogen oxides. Notably, PAN has been observed at unexpectedly high concentrations (maximum: 3.04 ppb) during the summertime. The average daily values of PAN showed a strong correlation with black carbon (BC) (R=0.77) and O_3 (R=0.77), suggesting a close connection between summertime haze and photochemical pollution. We addressed the puzzle of summertime PAN formation and its association with aerosol pollution under high O_3 conditions in Xiamen, a coastal city in southeastern China, by analyzing continuous high temporal resolution data utilizing box modeling in conjunction with the master chemical mechanism (MCM) model. The MCM model, with an index of agreement (IOA) value of 0.75, effectively investigate PAN formation, permorming better during the clean period (R^2: 0.68, slope K: 0.91) than haze one (R^2: 0.47, slope K: 0.75). Using extreme gradient boosting (XGBoost), we identified NH_3, NO_3^-, and $PM_{2.5}$ as the primary factors for simulation bias. Moreover, the net production rate of PAN becomes negative with PAN constrained, suggesting

an unknown compensatory mechanism. Both relative incremental reactivity (RIR) and empirical kinetic modeling approach (EKMA) analyses indicate that PAN formation is VOC-controlled. Controlling emissions of VOCs, particularly alkenes, C_5H_8, and aromatics, would mitigate PAN pollution. PAN promotes OH and HO_2 while inhibiting the formation of O_3, RO_2, NO, and NO_2. This study deepens our comprehension of PAN photochemistry while also offering scientific insights for guiding future PAN pollution control strategies.

Introduction

PAN is a significant secondary gaseous pollutant commonly present in photochemical smog and poses risk to human health and plant growth, being 1-2 magnitudes more phytotoxic than O_3 (Yukihiro et al., 2012; Taylor, 1969). Additionally, PAN's low aqueous solubility, minimal reactivity with hydroxyl radicals (OH), and slow photolysis contribute to its capacity for long-range transport of nitrogen oxides (NO_x) (Xu et al., 2018; Zhai et al., 2024; Marley et al., 2007b). Therefore, its formation in polluted areas holds significant importance beyond local concerns. Similar to surface O_3, PAN is produced during the oxidation of VOCs in the presence of NO_x (R1-R3) (Xu et al., 2021). PAN is formed when NO_2 reacts with peroxyacetyl (PA) radicals ($CH_3C(O)OO\cdot$) (R2), but the presence of NO consumes PA radicals, inhibiting PAN production (R3), which creates a comparable dependence of PAN and O_3 on NO and NO_2 levels. Unlike O_3, however, PAN is influenced by only a limited number of oxygenated VOCs (OVOCs) that generate PA radicals. These OVOCs, which are second-generation precursors of PAN, include acetaldehyde (CH_3CHO), acetone ($CH_3C(O)CH_3$), methylglyoxal (MGLY, $CH_3C(O)CHO$), methyl vinyl ketone (MVK, $CH_2CHC(O)CH_3$), methyl ethyl ketone (MEK, $CH_3C(O)CH_2CH_3$), methacrolein (MACR, $CH_2C(CH_3)CHO$), and biacetyl ($CH_3C(O)C(O)CH_3$). These compounds are typically formed from the oxidation of alkenes, aromatics, and isoprene, which are the first-generation precursors of PAN (Xue et al., 2014; Zhang et al., 2015). Identifying the dominant precursors is crucial for managing PAN pollution effectively. In the troposphere, thermal decomposition (R4) is the primary process responsible for PAN loss.

$$VOC_s + hv/OH/O_3/NO_3 \xrightarrow{O_3} CH_3C(O)OO\cdot + products \quad \text{R1}$$

$$CH_3C(O)OO\cdot + NO_2 \xrightarrow{k_2} PAN \quad \text{R2}$$

$$CH_3C(O)OO\cdot + NO \xrightarrow{k_3} CH_3\cdot + NO_2 + CO_2 \quad \text{R3}$$

$$PAN \xrightarrow{k_4} CH_3C(O)OO\cdot + NO_2 \quad \text{R4}$$

In recent years, wintertime photochemical air pollution has increasingly garnered attention. At this time, the concentration of O_3 is low due to the strong titration of NO, while the concentration of aerosol is high, and it is found that aerosol promotes PAN generation (Xu et al., 2021). Surprisingly high concentrations of OH radical, particularly under hazy conditions, have been observed and are largely attributed to HONO photolysis (Xu et al., 2021). Winter photochemical and haze pollution often exacerbate each other, with photochemical trace gases supplying both oxidants and precursors for aerosol formation, and aerosols acting as mediums for

heterogeneous reactions that produce key oxidants such as HONO, H_2O_2, and OH radicals (Xu et al., 2021). The OH produced by HONO photolysis can partially replace the UV action to promote PAN formation in winter in southeast coastal area of China when particulate matter is high (≥35μg·m^{-3}) (Hu et al., 2020). Zhang et al. (2020) found the potential HONO sources significantly improved the PAN simulations in wintertime heavy haze events with high concentrations of PAN. High concentrations of PAN are a consequence of the increased levels of precursors and HONO observed during haze episodes (Liu et al., 2018). In conclusion, most previous studies have studied the effect of aerosol on PAN generation in winter. Further research on PAN should determine whether particulates significantly contribute to its formation during warmer seasons with elevated O_3 concentrations (Xu et al., 2021). In Eastern China, photochemical air pollution often involves high concentrations of both O_3 and PAN, a persistent issue during the warm season (April-September) for many years (Lu et al., 2020). The characteristics and formation pathways of PAN during summer have been increasingly studied in regions such as the North China Plain (NCP), the Yangtze River Delta, the Pearl River Delta, and southwestern China. These studies have generally shown consistent diurnal patterns and strong correlations between PAN and O_3, identifying acetaldehyde—primarily derived from the degradation of aromatics and alkenes—as the key direct precursor of PAN in the summer. However, there has been limited research on the formation of PAN and its relationship with aerosol pollution during the summertime.

Xiamen is one of the fastest urbanizing regions in the southeast China and is also one of the cities with the best air quality in China, where the air quality could represent the future of other Chinese urban regions. Between 2018 and 2023, Xiamen ranked among the top 10 cities in China, achieving positions of 7th in 2018, 4th in both 2019 and 2020, 6th in 2021, 9th in 2022, and returning to 7th in 2023 (mee.gov.cn, last assessed October 30, 2014). Xiamen is located in a low-latitude coastal area, with abundant sunlight and long daylight hours during the summer, resulting in strong solar radiation and rapid photochemical conversion rates. The city is typically influenced by the East Asian monsoon and serves as a transport channel for atmospheric pollutants from both the Yangtze River Delta and Pearl River Delta regions. Additionally, during the summer, Xiamen is often affected by complex meteorological conditions such as typhoons and the West Pacific Subtropical High (WPSH). The WPSH creates weather conditions that promote the formation and accumulation of photochemical pollutants and particulate matter (Wu et al., 2019). This setting provides an ideal "laboratory" for investigating the complexities of summertime PAN formation and its relationship with aerosol pollution under high O_3 concentrations. In summer, especially in July, high temperatures, high humidity, and intense radiation are likely to accelerate both the formation and consumption rates of PAN. In this study, continuous measurements of trace gases, substances related to aerosols, photolysis rate constants and meteorological parameters were performed at a suburban site in Xiamen from 10 to 31 July 2018. Firstly, we provide an overview of pollutant concentrations, meteorological parameters, and weather conditions during the observation period. Secondly, we simulate PAN concentration with the aid of box modeling combined with master chemical mechanism (MCM) model. Using machine learning with XGBoost, we identified the key factors that affect the observation-based model (OBM) model's simulation results and clarified the mechanisms linking haze pollution to photochemical air pollution, as

indicated by PAN and O_3. Thirdly, the study identified the main precursors and oxidants responsible for summertime PAN production in Xiamen and evaluated the influence of PAN on local atmospheric oxidation capacity. This study further emphasized the interplay between haze and photochemical air pollution and highlighted significant implications for future research.

2 Methodology

2.1 Field observations

Trace gases (including PAN, O_3, HONO, HNO_3, HCl, NH_3, VOCs, NO_x, CO, and SO_2), substances related to aerosols (including BC, PM_1, $PM_{2.5}$, PM_{10}, SO_4^{2-}, NO_3^-, NH_4^+, Cl^-, Na^+, K^+, Ca^{2+}, Mg^{2+}), photolysis rate constants (including JO^1D, JNO_2, JHONO, JHCHO_M, JHCHO_R, JNO_3_M, JNO_3_R, JH_2O_2), and meteorological parameters (including temperature, relative humidity, atmospheric pressure, wind speed, and wind direction) were continuously measured at an suburban site in Xiamen from 10 to 31 July 2018. All instruments were placed inside an air-conditioned container situated on the rooftop of a 20-story building at the Institute of Urban Environment, Chinese Academy of Sciences (IUE: 118.06° E, 24.61° N) (Fig. S1(a)). When southerly winds prevailed, Xiamen Island, characterized by dense population and traffic congestion, was located upwind of the IUE (Fig. S1(b)). The IUE supersite is surrounded by Xinglin Bay, several universities and institutes, and major roadways with heavy traffic, such as Jimei Road (< 200 m), Shenhai Expressway (870 m), and Xiasha Expressway (2300 m) (Fig. S1(c)).

PAN measurements were conducted using a PANs-1000 analyzer (Focused Photonics Inc., Hangzhou, China), which features an automated system consists of a gas chromatograph, an electron capture detector, and a calibration unit. The analyzer provided PAN readings every 5 minutes, with a detection limit of 50 ppt. The uncertainty and precision of the PAN measurements were ±10 % and 3 %, respectively. The PAN standard gas was produced through the reaction of acetone and NO under UV light. Calibration procedures included monthly multi-point calibrations and weekly single-point calibrations. Detailed information about the PAN detection system and calibration can be found in previous studies (Hu et al., 2020; Liu et al., 2022a). The VOC measurements were conducted using a gas chromatography mass spectrometer (GC-FID/MS, TH-300B, Wuhan, China) at an hourly time resolution. Detailed information regarding the VOC detection system and calibration procedures is available in our previous study (Liu et al., 2022b). HONO measurements were conducted using a customized Incoherent BroadBand Cavity Enhanced Absorption Spectroscopy (IBBCEAS) system developed by the Anhui Institute of Optics and Fine Mechanics (AIOFM), Chinese Academy of Sciences. The HONO detection limit was 100 ppt, with a time resolution of 1 minute. The measurement principle and calibration method of IBBCEAS can be found in the previous literature (Hu et al., 2022; Duan et al., 2018; Hu et al., 2024). The concentrations of inorganic components in $PM_{2.5}$ aerosols (including SO_4^{2-}, NO_3^-, NH_4^+, Cl^-, Na^+, K^+, Ca^{2+}, Mg^{2+}), as well as the concentrations of gases such as NH_3, HCl, and HNO_3 were analyzed using a Monitor for AeRosols and Gases in ambient Air (MARGA, Model ADI 2080, Applikon Analytical B.V., the Netherlands) (Hu et al., 2022). The criteria air pollutants O_3, NO_x, CO, and SO_2 were measured using different methods: ultraviolet (UV) absorption for O_3 (TEI model 49i), chemiluminescence with a molybdenum converter for

NO_x (TEI model 42i), non-dispersive infrared for CO (TEI model 48i), and pulsed UV fluorescence for SO_2 (TEI model 43i). A tapered element oscillating microbalance (TEOM1405, Thermo Scientific Corp., MA, USA) was used to continuously measure the mass concentrations of PM_1, $PM_{2.5}$, and PM_{10} online. A photolysis spectrometer (PFS-100, Focused Photonics Inc., Hangzhou, China) was employed to measure the photolysis rate constants. An ultrasonic atmospherium (150WX, Airmar, USA) was used to measure meteorological parameters.

2.2 Box modeling

This study employed a box model framework utilizing the Master Chemical Mechanism (MCMv3.3.1, https://mcm.york.ac.uk/MCM/home.htt) to investigate sensitivity and mechanisms of PAN formation. The model constraints were derived from observations of trace gases and meteorological parameters, which were averaged to 1-hour intervals. The reliability of model simulation results is often assessed using the index of agreement (IOA), which ranges from 0 to 1, with a higher IOA signifying greater alignment between observed and simulated values. Note that the model simulation values at this time are not constrained by PAN. For specific formulas, please refer to the supplementary information (Eq. S1). Other formulas, including PAN production rates (P(PAN)), net production of PAN (Net (PAN)), and the RIR, are provided in the supplementary information (Eq. S2- Eq. S4).

The MCM simulates the nonlinear interaction between PAN and its precursors by altering the VOCs-to-NO_x ratio across multiple scenarios, while keeping all other parameters fixed. In this study, a 20 % step size was applied, reducing VOCs and NO_x from 200 % down to 0 % to construct a scenario matrix. A total of 121 scenarios were generated to model the PAN production rate. The scenario representing the average VOCs and NO_x mixing ratio during the sampling period was designated as the base case, with the remaining 120 scenarios created by systematically adjusting the VOC-to-NO_x ratio. The output from these 121 simulations was used to construct isopleth diagrams depicting the relationship between VOCs, NO_x, and PAN.

2.3 Machine Learning Model

To identify the key factors influencing the performance of the model simulation, the Machine Learning (ML) model was applied to establish the prediction model of bias between simulation of OBM and observation. XGBoost is a supervised boosting algorithm that reduces the risk of over-fitting, captures the nonlinear relationships among predictor variables, and solves numerous data science problems in a rapid and accurate way (Li et al., 2024). It has demonstrated high performance in O_3 studies in China. As compared to other bagging tree models like random forest, XGBoost can handle more complex data while consuming fewer computing resources. To further improve the interpretability of the ML model, the feature importance of independent input variables in the XGBoost model is quantified using the Shaply Additive explanation (SHAP) approach (Lin et al., 2024). The SHAP calculates a value that represents the contribution of each feature to the model's outcome, which has been successfully applied in atmospheric environmental studies (Li et al., 2024; Lin et al., 2024). When the model was being adjusted, 90 % of the data was used as the

training data set, and 10 % of the data was used as the test data set. The hyperparameters were tuned using grid search and cross-validation method. Specifically, for a single hyperparameter, grid search was used to obtain its more appropriate value range, and for the combinations of hyperparameters, the whole training set was split into ten folds and then run a grid search over pre-adjusted combinations of hyperparameters by training nine folds and predicting on the one fold in cross-validation procedure. For key hyperparameters of XGBoost model, the number of trees was 100, learning rate was 0.1, max depth was 6. The model was trained and tested on hourly data during the whole observation and the established model was examined by coefficient of determination (R^2) value, the root-mean-squared error (RMSE) and mean absolute error (MAE). The formulas of RMSE and MAE are provided in the supplementary information (Eq. S5 & Eq. S6). The performance of both models is illustrated in Fig. S3. The R^2, MAE, and RMSE for the training set are 0.90, 0.08, and 0.12, respectively, while the corresponding values for the test set are 0.77, 0.10, and 0.14, respectively. These statistical metrics indicate that the XGBoost model is promising for further analysis.

3. Results and discussion

3.1 Overview of observation

The measured data of PAN, related trace gases and meteorological parameters at IUE over 10 to 31 July 2018 are documented in Fig. 1. Combined with the synoptic situation shown in Fig. S4, the 8th typhoon of 2018, Typhoon Maria, made landfall on the morning of the 11th at Huangqi Peninsula in Lianjiang County, Fujian. Due to the influence of the typhoon's outer spiral rain bands, there was moderate to heavy rain on the 11 July 2018. Correspondingly, there was a noticeable decrease in ultraviolet radiation and the temperatures. Starting from the 12 July 2018, a WPSH strengthened and extended westward, exerting control over Xiamen. In the lower atmosphere, it was influenced by the eastward flow, resulting in predominantly cloudy weather. From the 16 to 18 July 2018, the area was affected by the outer periphery of Typhoon Shan Shen, which formed on the 17 July 2018, in the northeastern part of the South China Sea and moved westward, making landfall along the coast of Wancheng Town, Wanning City, Hainan Province in the early hours of the 17 July 2018. During this period, the city experienced strong winds with gusts reaching 5 to 6 on the Beaufort scale in the urban areas. At the same time, the concentration of various pollutants reached their lowest levels, and the daily variation patterns were less pronounced. From the 20 to 21 July 2018, Xiamen experienced the influence of the peripheral descending airflow associated with Typhoon Ampil (which formed in the northwest Pacific Ocean around 8:00 PM local time (LT) on the 18 July 2018, and moved northwest, making landfall along the coast of Chongming Island, Shanghai, around noon on the 22 July 2018). During this period, there were fewer clouds and higher temperatures. From the 22 to 24 July 2018, the city was successively affected by the outer periphery of Typhoon Ampil and a tropical low-pressure system, resulting in occasional showers or thunderstorms. From the 25 to 31 July 2018, a WPSH once again strengthened and controlled Xiamen. As a result, Xiamen experienced stable meteorological conditions, with light winds (ws = 1.04 m s), persistently high temperatures (maximum daily average of 37.82 °C), and high relative humidity (maximum daily average of 81.65 %). These factors created an environment that

favored the buildup of particulate matter and enhanced the photochemical formation of O_3 and PAN (Wu et al., 2019). The maximum daily average of $PM_{2.5}$, O_3 and PAN were 49.26 μg.m^{-3}, 93.62 ppb, and 1.37 ppb, respectively.

The phenomenon of simultaneous high levels of photochemical and particulate matter appears. Throughout the 22-days campaign, 12 days (including 11, 13, 21-23, and 25-31 July 2018) were observed with 1 h concentrations of $PM_{2.5}$ exceeding 35 μg m^{-3}; 13 days (including 11, 13, 15, 20-23, and 26-31 July 2018) were observed with 5-min concentrations of PAN exceeding 1 ppb. The maximum concentration was recorded at 3.04 ppb (5-min data) at 11:09 LT of 13 July 2018. This concentration of PAN is comparable to the levels recorded at downwind of Guangzhou, southern China (3.9 ppb, Wang et al., 2010), 2.51 ppb in Nashville, U.S (Roberts et al., 2002). However, this value was significantly lower than heavily polluted areas in northern China in the summer, such as Beijing (9.34 ppb, Xue et al., 2014), Lanzhou (9.12 ppb, Zhang et al., 2009), and Jinan (13.47 ppb, Liu et al., 2018). This is likely because the higher summer temperatures in the southeastern coastal region are conducive to the thermal decomposition of PAN, and the precursor concentrations of PAN, including NO_2 and VOCs, are significantly lower in the studied area compared to those in the northern region. The concentration of alkanes is the highest, followed by alkenes, OVOCs and aromatics, while halogenated hydrocarbons and C_5H_8 exhibit lower concentrations (Fig. S5). Furthermore, VOC concentrations for various species are elevated during haze periods compared to clean periods (Fig. S5). Table S1 provides the detailed VOC concentrations observed during the study period. Throughout the observation period, the variations in O_3 and PAN were almost identical, but the maximum concentration of O_3 occurred at 3:00 PM LT on 29 July 2018 (114.12 ppb). The correlation between the average daily values of PAN and both BC and O_3 is strong, with a correlation coefficient of 0.77 for each (Fig. S6), suggesting that summertime haze and photochemical pollution were deeply connected.

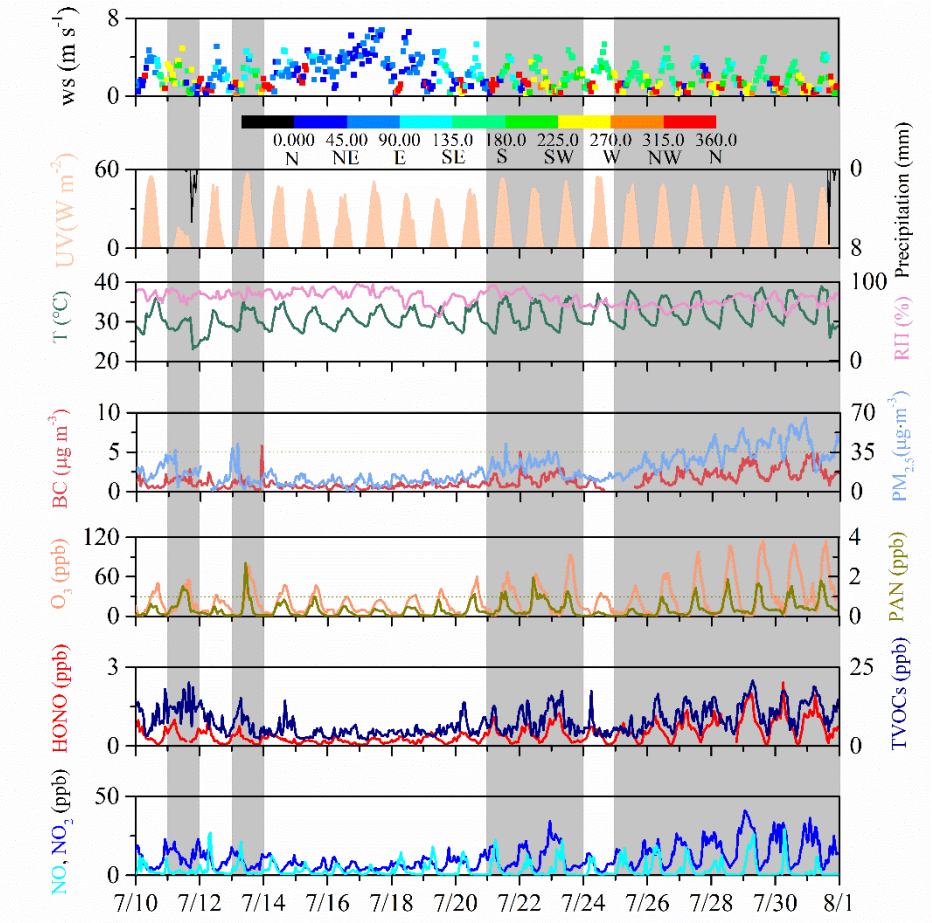

Figure 1. Time series of trace gases and meteorological parameters observed at IUE during 10-31 July 2018. The gray shading represents days when the $PM_{2.5}$ hourly daily maximum value exceeded 35 μg m^{-3}.

We categorize it as "haze" and "clean" based on whether the $PM_{2.5}$ hourly daily maximum value is greater than 35 μg m^{-3}. Specifically, "haze" includes 11, 13, 21-23, and 25-31 July 2018, while other days are categorized as 'clean'. To provide a quantitative perspective, the statistics for PAN and associated species were calculated and compiled in Table 1. $PM_{2.5}$ concentrations during the haze period were significantly higher than those during the clean period, being 2.49 times those of the clean period. There was no significant difference of UV levels between clean and haze periods, while temperatures in the haze phase were notably higher than those in the clean phase. Therefore, without considering precursors, PAN concentrations should be lower during the haze phase due to higher thermal decomposition. In fact, PAN concentrations during the haze period were 2.35 times higher than those during the clean period. During the haze period, O_3 concentrations were also significantly higher than those during the clean period, being 2.04 times those of the clean period. These observations indicate that the atmospheric oxidation capacity is relatively strong during the haze period. Similar to PAN, HONO also exhibits higher concentrations during the haze phase (approximately 2.33 times that of clean conditions), which is consistent with current research findings that particles promote the generation of HONO (Ye et al., 2017). NO also experienced an increase from clean (3.28 ppb) to hazy (4.30 ppb) conditions, albeit less prominently than NO_2 (from 7.21 to 14.55 ppb). This observation further underscores that, during hazy periods, the

atmosphere demonstrates heightened oxidizing potential, facilitating the conversion of NO to NO_2. While the increased NO levels on hazy days reduced PA radicals and hindered PAN formation, this effect was offset by the concurrently higher concentrations of PAN precursors (NO_2 and VOCs) during those days. The TVOCs have increased to some extent, but in hazy conditions, they are only 1.34 times that of clean conditions. This is also because the strong oxidizing conditions during haze periods convert VOCs into secondary pollutants, such as O_3 and PAN. Although it is acknowledged that VOCs can also be converted into secondary organic aerosol (SOA), the discussion of SOA is beyond the scope of this study. The TVOC levels at this site are comparable to that at a rural site in a coastal city-Qingdao (7.6 ppb), significantly lower than inland sites, such as Wuhan (30.2 ppb, Liu et al., 2021a) and Chengdu (28.0 ppb, Yang et al., 2020) or economically more developed coastal cities, such as Shanghai (25.3 ppb, Zhu et al., 2020) and Hong Kong (26.9 ppb, Wang et al., 2018), and significantly higher than regional background locations like Mt. Wuyi (4.7 ppb, Hong et al., 2019) and Mt. Nanling (4.7 ppb, Wang et al., 2023), and global background station Mt. Waliguan (2.6 ppb, Xue et al., 2013). The isoprene level during haze period was significantly higher than that during clean period probably due to haze period with higher temperature (Wang et al., 2023). The wind speed was very low during both the clean and haze periods, especially during the haze period with only 1.12 m s^{-1}. The relative humidity was high during both periods, and there was no significant difference between the clean and haze periods.

Table 1. Descriptive statistics of major trace gases (ppb), particulate matter (μg m^{-3}) and meteorological parameters during 10-31 July 2018.

Species	Clean (mean ± SD)	Haze (mean ± SD)
PAN	0.20 ± 0.23	0.47 ± 0.46***
O_3	16.07 ± 12.73	32.79 ± 29.73***
HONO	0.27 ± 0.18	0.63 ± 0.43***
NO	3.28 ± 4.03	4.30 ± 8.39***
NO_2	7.21 ± 3.87	14.55 ± 8.89***
TVOCs	6.13 ± 1.73	8.19 ± 2.55***
C_5H_8	0.13 ± 0.04	0.17 ± 0.05***
PM_1	10.13 ± 3.91	24.36 ± 10.77***
$PM_{2.5}$	11.21 ± 5.33	27.93 ± 13.16***
PM_{10}	24.26 ± 9.45	47.28 ± 20.63***
UV (W m^{-2})	14.29 ± 17.38	13.18 ± 17.40
T (°C)	30.68 ± 2.39	31.92 ± 3.36***
RH (%)	81.94 ± 8.60	77.18 ± 8.22
WS (m s^{-1})	1.64 ± 0.69	1.12 ± 0.61*

Note: *, **, and *** indicate that they passed the significance test at 0.05, 0.01 and 0.001 levels, respectively.

The average diurnal patterns of PAN and related variables have been averaged separately for clean and hazy conditions (Fig. 2). The daily variation of PAN exhibits a clear unimodal pattern, with concentrations starting to rise after sunrise and decreasing after

12:00 LT caused by thermal decomposition of PAN at high temperatures (Fig. 2). Although PAN and O_3 exhibit a slight bimodal pattern during the clean period, this is primarily due to the bimodal pattern of UV during this time. The peak occurring at noon indicates that PAN primarily originates locally, as a delay of about 1-2 hours would be expected if it were influenced by transportation (Liu et al., 2024). The daytime increment was much larger for hazy condition (1.17 ± 0.44 ppb) than for clean condition (0.52 ± 0.21 ppb), indicating stronger photochemical production of PAN for hazy condition. The daily variation pattern of O_3 is similar to PAN, except that O_3 reaches its peak relatively later compared to PAN, with the peak occurring at 16:00 during the clean phase and 14:00 LT during the haze phase. Although PAN and O_3 are both products of photochemical reactions involving NO_x and VOCs, their production efficiencies differ. PAN is specifically formed from VOCs that are precursors to the acetyl radical (CH_3CO), whereas O_3 can be produced from the oxidation of any VOCs. Analyzing the correlation between PAN and O_3 can offer insights into their respective photochemical production efficiencies. As shown in Fig. S7, the positive correlation between the daily maximum values of PAN and O_3 for clean condition (R^2=0.67) was better than that for hazy condition (R^2=0.15). The slopes of the linear regression were 0.021 ppb/ppb for clean conditions and 0.009 ppb/ppb for hazy conditions. This indicates that, on average, approximately 2.1 ppb of PAN could be produced for each 100 ppb of O_3 formed under clean conditions, and about 0.9 ppb of PAN for each 100 ppb of O_3 under hazy conditions in the air masses reaching IUE. The slope of linear regression for clean condition is comparable to those determined in Hongkong (0.028, Xu et al., 2015), Mexico city (0.020, Marley et al., 2007a), and Nashville (0.025, Roberts et al., 2002). The lower efficiency of PAN production relative to O_3 indicates that PAN precursors represent only a small portion of the total VOCs, especially during hazy conditions. Additionally, the high temperatures in the southeast coastal region likely contribute to the lower production efficiency of PAN. The average temperature during the entire observation period was 31.39 °C, with an average temperature of 34.64 °C at 12:00 LT. This result is consistent with the result that RIR during the cleaning period is higher than that during the haze period. As shown in Fig. S8, in the clean period, the correlation between PAN and O_3 is the strongest (R^2=0.70), indicating that O_3 and PAN are both photochemical end products during clean periods. In contrast, during hazy periods, the correlation between PAN and $O_3 \times JO^1D$ is the strongest (R^2=0.66), suggesting that O_3 plays a more significant role in promoting PAN formation through photolysis to generate OH during hazy periods.

Unlike the daily variation patterns of PAN and O_3, HONO exhibits a swift concentration decrease after sunrise in both clean and hazy conditions, undergoing photolytic conversion into OH radicals. Subsequently, in clean conditions, HONO starts to increase in concentration after sunset. In hazy conditions, however, the increase begins from 16:00 LT and not after sunrise. This suggests a robust daytime net production or transport of HONO, where the rates surpass those of HONO photolysis and other sinks in the afternoon in hazy conditions. The NO levels reach their peak at 7:00 LT during the morning rush hour, reflecting advection of fresh urban plumes to the study site. The daily variation of NO_2 exhibits a 'U' shape, reaching its minimum value at 13:00 LT, mainly owing to effects of emission, boundary layer height and photochemical reactions. In the clean period, the daily variation of $PM_{2.5}$ is similar to that of NO_2, both showing a 'U' shape, reaching their lowest values at noon. However, during the haze phase, the daily

variation pattern of $PM_{2.5}$ appears somewhat different. There is a noticeable trough in the early morning, remains stable during the day, and starts to rise after sunset. The diurnal variation of VOC concentrations for various species are not significant during clean periods (Fig. 2(e)), likely due to higher wind speeds that facilitate the dispersion of pollutants. In contrast, during haze periods, the daily variations are evident, with peaks occurring before sunrise, followed by a decline, and then an increase after sunset (Fig. 2(f)). This is because the haze period is relatively stable at nighttime, which allows for the accumulation of pollutants, while during the daytime, sunlight converts VOCs into photochemical products like O_3 and PAN.

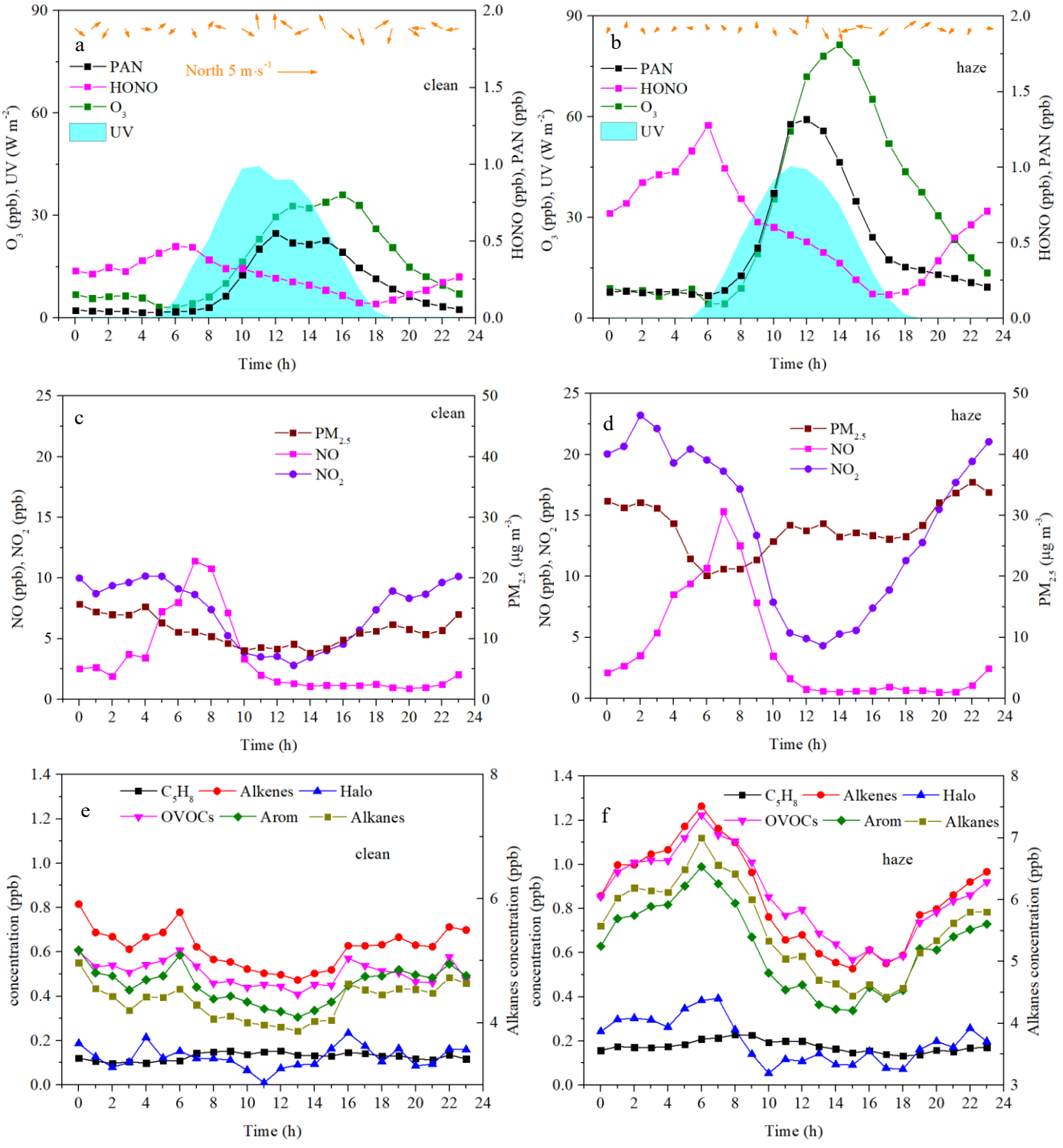

Figure 2. The diurnal variations of PAN, HONO, O_3, and UV during clean (a) and hazy (b) periods, the diurnal variations of $PM_{2.5}$,

NO, and NO_2 during clean (c) and hazy (d) periods, and the diurnal variations of isoprene (C_5H_8), Alkenes, halogenated hydrocarbons (Halo), OVOCs, aromatics (Arom), and alkanes during clean (e) and hazy periods (f).

3.2 PAN formation: key factors and mechanisms

To investigate the key factors and mechanisms of PAN formation, PAN was simulated by constraining the MCM-based box model with meteorological conditions and observed concentrations of precursor gases. The model successfully replicated the variations in PAN, achieving an IOA of 0.75 (Fig. 3(a)), which was within the accepted range (0.66-0.87) in previous studies (Zeng et al., 2019). The model captured its formation rate in general well, with observed rates varying from 0.04 to 0.52 ppb·h^{-1} (average: 0.20 ppb·h^{-1}) and modeled rates ranging from 0.09 to 0.46 ppb·h^{-1} (average: 0.19 ppb·h^{-1}) (see Fig. 3(b)). The similar result was found in the North China Plain (NCP) region in the wintertime (Xu et al., 2021). When calculating the IOA separately for clean and hazy periods, it was found that the IOA significantly increased to 0.89 and 0.81 (Fig. 3(c)), respectively. This phenomenon indicates a substantial difference in the PAN production and destruction mechanisms between clean and hazy periods. Furthermore, the simulated values are closer to the observed values during clean period, reflected in a higher R^2 value (R^2=0.68) and a slope value (K) closer to 1 (K=0.91) (Fig. 3(c)). In contrast, the R^2 value and the K value during hazy period are only 0.47 and 0.75, respectively (Fig. 3(c)). This phenomenon suggests that some reactions related to PAN generation or destruction might be missing in the MCM during the hazy period.

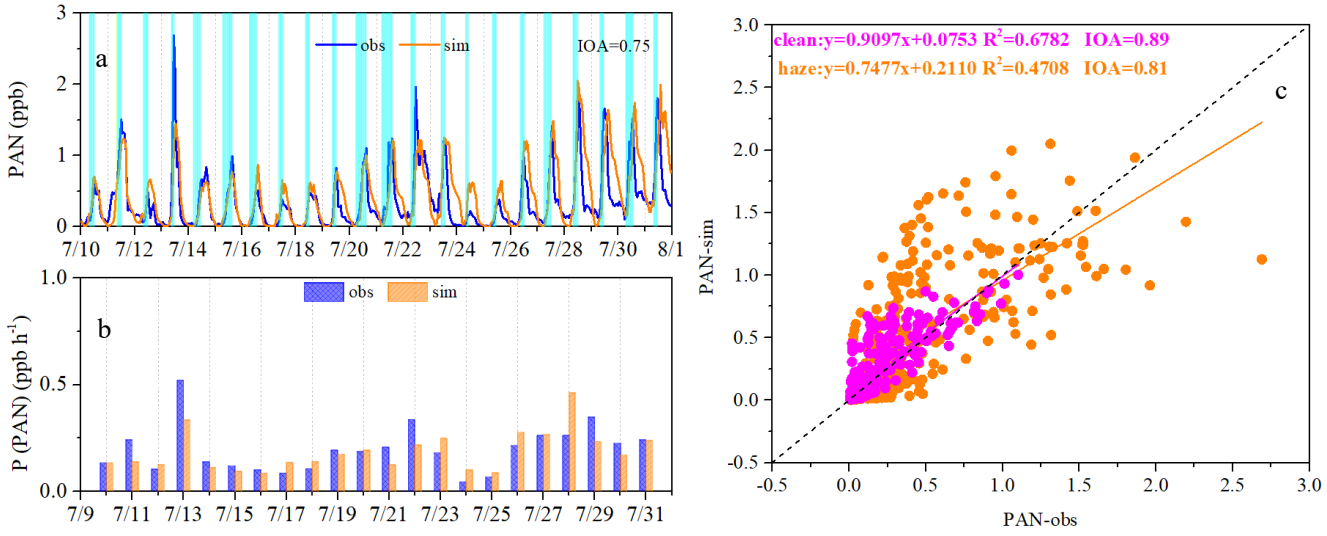

Figure 3. Comparisons of observed (obs) PAN and simulated (sim) PAN (daytime photochemical PAN production periods indicated by cyan shading), (b) production rates, (c) correlation between PAN observations and simulated values.

To identify the key factors influencing the performance of the OBM model simulation, the bias (the model simulation minus the observed value) as the target. The remaining variables, which were not input into the OBM model, such as NH_3, HNO_3, HCl (alkaline and acidic gaseous pollutants), $PM_{2.5}$ concentrations and their components, as well as physical process parameters like wind speed and wind direction, were used as features. As shown in Fig. 4 (a), through XGBoost-SHAP machine learning, we found

that NH_3 is the most significant parameter affecting bias, contributing 19.68 % (Fig. S9). A scatter plot analysis of the SHAP values of NH_3 versus NH_3 concentrations revealed that as NH_3 concentrations increase (Fig. 4 (b)), the OBM model tends to overestimate PAN concentration more significantly. To date, there are very few studies that directly address the impact of NH_3 on PAN formation. Xu et al. (2021) suggested that NH_3 could promote the formation of HONO, which in turn affects PAN formation. However, since we included HONO as an input to constrain the model, the indirect influence of NH_3 on PAN formation through HONO can be excluded. NH_3 in the atmosphere can preferentially react with sulfuric acid (H_2SO_4) to form ammonium sulfate ($(NH_4)_2SO_4$) secondary inorganic aerosols (Behera et al., 2013), leading to the heterogeneous reaction removal of PAN by secondary inorganic aerosols (Pratap et al., 2021). This result is validated by the positive correlation between the SHAP values of NH_4^+ and SO_4^{2-} and their respective concentrations (Fig. S10). NO_3^- is the second most significant parameter influencing the bias between the two, contributing 11.33 % (Fig. S9). NO_3^- has a negative correlation with the bias (Fig. 4 (c)), indicating that higher NO_3^- levels lead to more significant underestimation by the model. Considering the significant positive correlation between PAN and NO_3^- at the 0.01 level, with a correlation coefficient of 0.37, and the fact that both reach their peaks around noon (Fig. S11), it is likely that they have a common source. $PM_{2.5}$ is the third most significant parameter (Fig. 4 (a)), contributing 9.40 % (Fig. S9). $PM_{2.5}$ has a positive correlation with the bias (Fig. 4 (d)), indicating that higher $PM_{2.5}$ levels lead to more significant overestimation by the model, suggesting that PAN can undergo heterogeneous removal on the surface of $PM_{2.5}$ in the actual atmosphere (Sun et al., 2022).

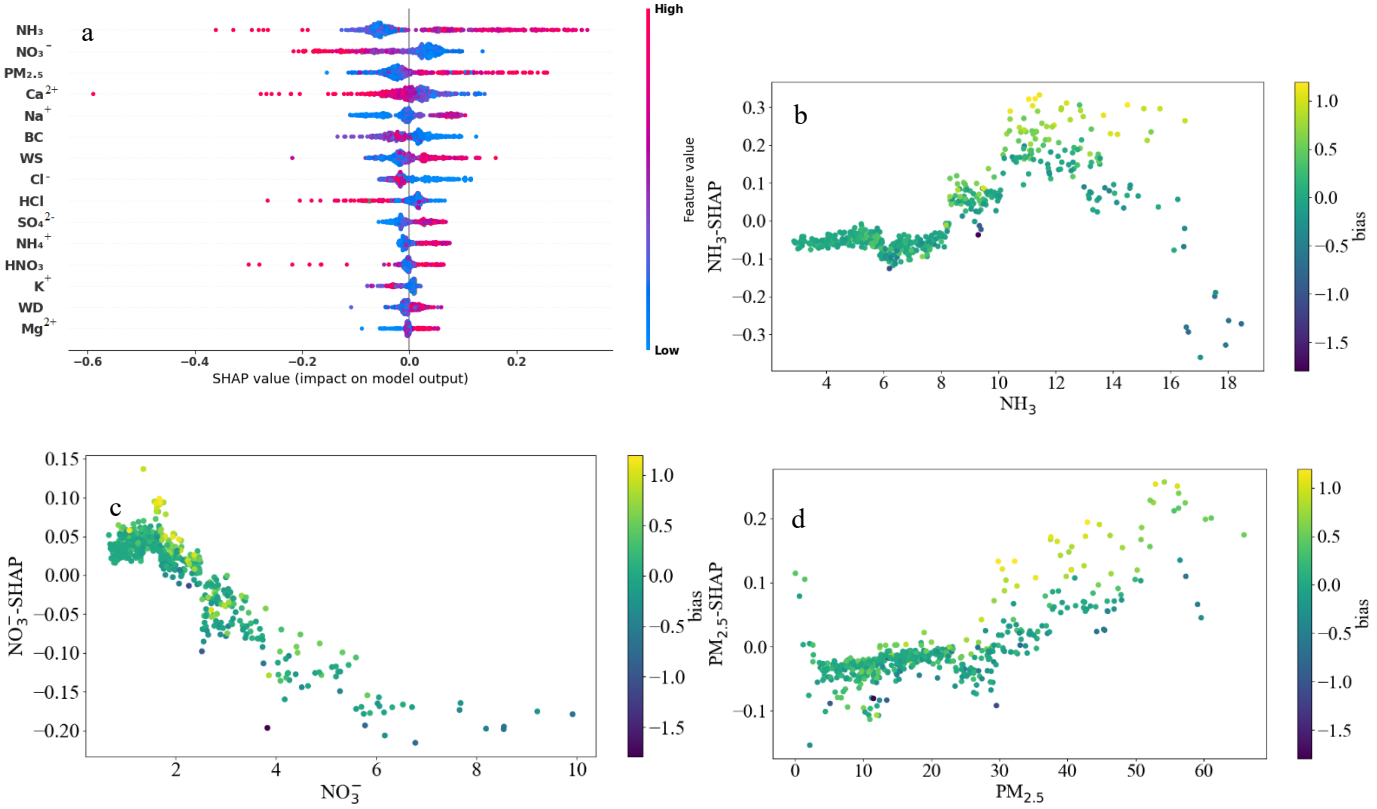

Figure 4. Feature importance was obtained by XGBoost-SHAP method (a). The scatter plots between concentration of top three important features and their SHAP values (b, c and d), and colored with the bias (the model simulation minus the observed value).

Figure 5 (a) and (b) show the average production and destruction rates of PAN during clean and haze periods, as simulated by OBM without PAN constrained. During the haze period, both the production and destruction rates of PAN are significantly higher than during the clean period. The higher production rate of PAN during the haze period is due to the higher concentration of PAN precursors, while the higher destruction rate is because both the temperature and PAN concentration are higher. Regarding the net production rate, it is also higher during the haze period than during the clean period, which corresponds to the previously observed diurnal variation. From 6:00 to 12:00 LT during the haze period, the simulated net production rate of PAN is positive, with an average value of 0.19 ppb h^{-1}. During the clean period, from 6:00 to 12:00 LT, the simulated net production rate of PAN is 0.12 ppb h^{-1}. The observed diurnal variation of PAN shows that from 6:00 to 12:00 LT, the average net production rates during the haze and clean periods are 0.20 ppb h^{-1} (Fig. 2(a)) and 0.09 ppb h^{-1} (Fig. 2(b)), respectively. The model-simulated net production rate is close to the observed net production rate, further indicating that the model can simulate PAN well, and also confirming that PAN in summer mainly comes from local production. The net production rate of PAN during the haze period is similar to the summer results in urban areas of the Pearl River Delta (PRD), which is 0.17 ppb h^{-1}, while the net production rate of PAN during the clean period is similar to the summer results in rural areas of the PRD, which is 0.12 ppb h^{-1} (Liu et al., 2024).

Figure 5 (c) and (d) show the average production and destruction rates of PAN during clean and haze periods, as simulated by OBM with PAN constrained. The net production rate of PAN is approximately zero at night during both clean and haze periods, while there is a significant difference in the net production rate during the day. During the clean period, the daytime net production rate of PAN is greater than zero, with an average value of 0.19 ppb h^{-1}. In contrast, during the haze period, the net production rate of PAN is negative from 6 AM to 1 PM LT, with an average value of -0.47 ppb h^{-1}, and positive from 2 PM to 5 PM LT, with an average value of 0.47 ppb h^{-1}. Previous research has shown that an increase in temperature, an increase in PAN concentration, or a decrease in PAN precursors (including VOCs and NO_2) can cause the net production rate of PAN to change from positive to negative (Liu et al., 2024). We conducted a correlation analysis of the net production rate of PAN with temperature, PAN, VOCs, and NO_2 concentration and found that the net production rate of PAN had the best correlation with PAN concentration (R^2=0.13), showing a significant negative correlation (k=-0.53, Fig. S12). Additionally, we also observed that when the net production rate of PAN is negative, the PAN concentration is often very high (Fig. S12). As shown in Fig. 6, we conducted sensitivity experiments by reducing the PAN concentration by 80 %, i.e., 0.2 times the observed value, and found that the simulated net production rate of PAN was positive throughout the observation period. Conversely, when the PAN concentration was increased by 140 %, i.e., 2.4 times the observed value, the simulated net production rate of PAN was found to be almost negative throughout the observation period. Besides, we also conducted sensitivity experiments on temperature and found that when simulating winter temperatures, i.e., 0.4 times the observed value, with a temperature range of 9.25-15.29 °C, the simulated net production rate of PAN was positive throughout the observation period. Similarly, when simulating spring and autumn temperatures, i.e., 0.6 times the observed value,

with a temperature range of 13.87-23.39 °C, the simulated net production rate of PAN was also positive throughout the observation period. In conclusion, the simulated net production rate of PAN becomes negative with PAN constrained, further suggesting the existence of an unknown compensatory mechanism.

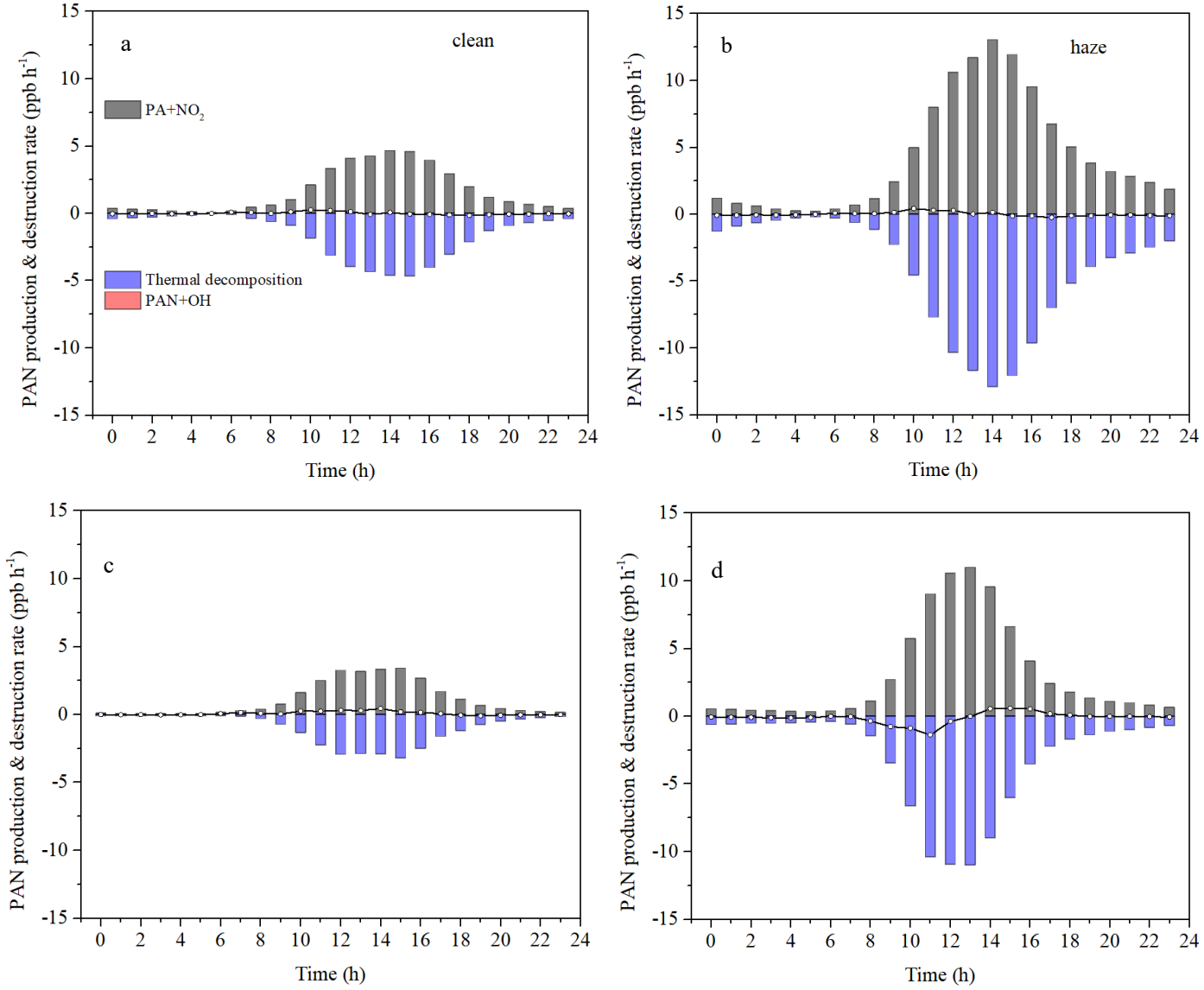

Figure 5. Average diurnal variation of the OBM simulated production, destruction and net rates of PAN during clean (a) and haze days (b) without PAN constrained. And average diurnal variation of the OBM simulated production, destruction and net rates of PAN during clean (c) and haze days (d) with PAN constrained.

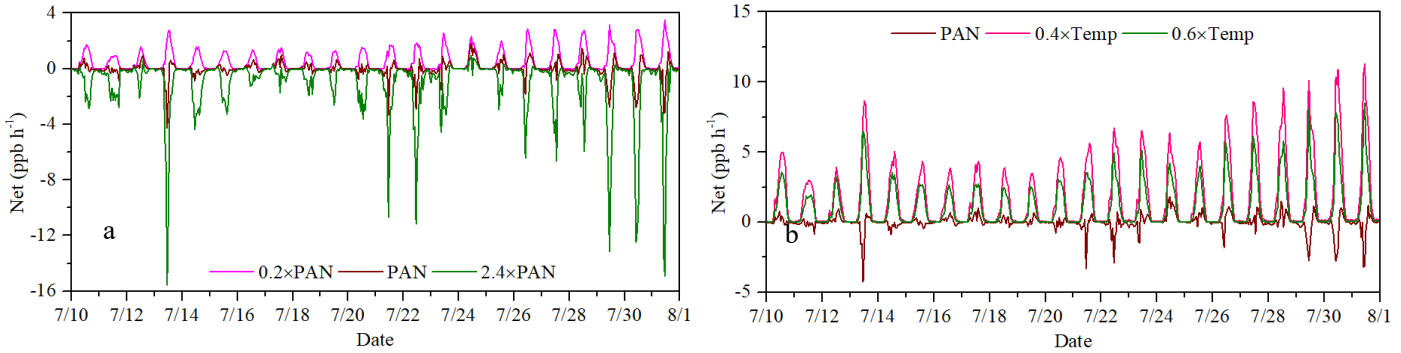

Figure 6. Net PAN production rates simulated by OBM at different PAN concentrations (a) and different temperatures (b).

PAN is formed when the PA radical reacts with NO_2. Given the swift equilibrium between R2 and R4 at high temperatures, budget analysis of PA's production and consumption pathways are frequently used to detail the mechanisms behind PAN formation (Sun et al., 2020; Liu et al., 2022a; Liu et al., 2024). Figure 7 illustrates the diurnal patterns of the primary production and loss pathways for the PA radical simulated by OBM across different periods. As shown in Fig. 7, during haze days, the rates of PA production and destruction were twice as high as those on clean days. This indicates that radical cycling and photochemical formation were more efficient during haze days, driven by higher temperatures and a greater abundance of precursors (Zeng et al., 2019). The PA radical production rate from PAN thermal decomposition reached its peak at 15:00 LT (3.22 ppb h^{-1}) and 13:00 LT (10.99 ppb h^{-1}) for clean and haze days, perfectly coinciding with the peak temperature time. In addition, the conversion of PAN into PA radical through thermal decomposition had high exponential correlations with temperature during both haze (R^2=0.95) and clean days (R^2=0.91) (Fig. S13). Previous laboratory experiments also indicated that the thermal decomposition of PAN is exponentially related to temperature (Cox & Roffey 1977; Senum et al., 1986; Tuazon et al., 1990). The conversion of PAN into PA radical through thermal decomposition during haze days was significantly higher than that during clean days, which was not only enhanced by higher temperature but also maintained by higher PAN concentration during haze days. The thermal decomposition of PAN to PA radical during the day (5:00-18:00 LT) accounted for 68.22 % and 45.59 % during haze and clean days, respectively. The pathways that did not account for the transformation between PA and PAN reached their peak around noon (11:00 LT), coinciding with the highest solar radiation and the most intense photochemical reactions, which has been observed in spring and autumn at the same site (Liu et al., 2022a).

Production rates of PA from other pathways related to precursors, including OVOCs, radical cycling, MGLY, and CH_3CHO, showed single-peak patterns around noon, which suggested that the PA radical generated from these pathways was primarily increased by intense solar radiation at noontime (Sun et al., 2020). The average day PA radical production rates from CH_3CHO via reactions with OH and NO_3 were 1.10 and 0.93 ppb h^{-1}, accounting for 48.85 % and 49.35 % (exclude PAN thermal decomposition sources) during haze and clean days, respectively. These percentages were comparable to previous studies in Guangzhou (46 %, Yuan et al., 2018) and Beijing (34.11-50.19 %, Xue et al., 2014), suburban site of Chongqing (47.72 %, Sun et al., 2020). The second production pathway involved MGLY undergoing photolysis and oxidation through reactions with OH and NO_3 (haze: 0.50 ppb h^{-1} and clean: 0.42 ppb h^{-1}), contributing to 22.27 % and 22.12 % for haze and clean days, respectively. Subsequently, radical cycling processes—including the decomposition of RO radicals and the reactions of acyl peroxy radicals with NO—were also significant contributors to PA production, accounting for 18.98 % on haze days and 19.54 % on clean days. PA from the other OVOCs (excluding CH_3CHO, MGLY) via photolysis and oxidation reactions involving OH, NO_3, and O_3, accounted for 9.90 % and 8.99 % during haze (0.22 ppb h^{-1}) and clean days (0.17 ppb h^{-1}). There were no notable differences in the proportions of individual pathways contributing to PA

between haze and clean days, indicating comparable pollutant compositions in the atmospheric around IUE (Zeng et al., 2019). In summary, the thermal decomposition of PAN played the dominant role in boosting PA production rates during both clean and haze periods, followed by contributions from CH_3CHO, MGLY, radical cycling, and other OVOCs. The primary contributor to the PA destruction rate was the reaction between PA and NO_2, accounting for 67.72 % and 51.09 % during haze (4.74 ppb h^{-1}) and clean days (1.76 ppb h^{-1}), respectively, followed by PA+NO, contributing to 32.28 % and 48.91 % during haze (2.26 ppb h^{-1}) and clean days (1.69 ppb h^{-1}), respectively.

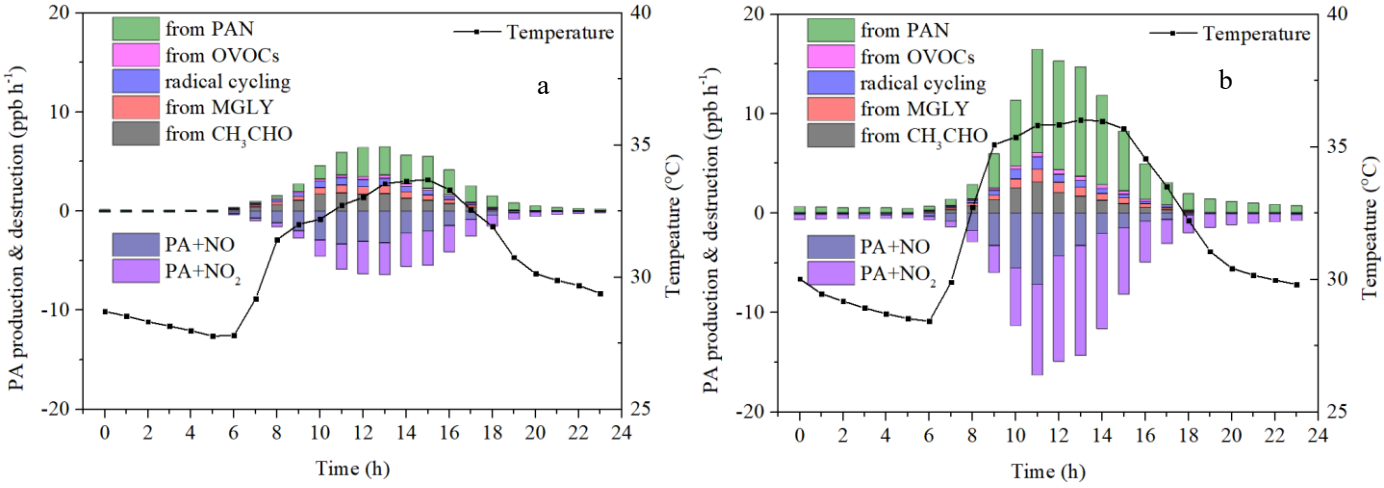

Figure 7. PA radical production and destruction pathways simulated by OBM on (a) clean days and (b) haze days.

3.3 Sensitivity of PAN formation and its impact on the local atmosphere

To determine the principal precursors influencing PAN formation, sensitivity modeling analyses were carried out to investigate how PAN relates to its precursors. The RIR reflects how sensitive PAN formation is to changes in its precursor levels. As shown in Fig.8 (a), the RIR of NO was negative, ranging from -0.67 to -0.27 (-0.52 ± 0.13) throughout the observation period. However, RIR is positive for other species, with NO_2 (0.50 ± 0.11) and VOCs (0.50 ± 0.15) having the highest RIR, followed by HONO (0.12 ± 0.04) and O_3 (0.10 ± 0.03). Around 50 types of VOCs were classified as alkanes, OVOCs, halogenated hydrocarbons (Halo), alkenes, aromatics (Arom), and isoprene (C_5H_8 representing biogenic hydrocarbons). Among these VOCs, the RIR of alkenes (0.22 ± 0.07) is the highest, followed by C_5H_8 (0.13 ± 0.04) and Arom (0.13 ± 0.04), while OVOCs (0.06 ± 0.01) and Halo (0.05 ± 0.01) have very low RIRs (Fig. 8 (b)). These phenomena indicated that increased NO level would inhibit the production of PAN while increased NO_2, VOCs (especially alkenes, C_5H_8, and Arom), HONO, and O_3 would promote the production of PAN. Because the values of NO and NO_2 RIR are approximately equal but with opposite signs, the RIR for NO_x is almost zero, indicating that the PAN generation at this site is not sensitive to NO_x. Zeng et al. (2019) also observed that NO_2 had a positive effect on PAN formation, while NO had a negative effect, in a suburban area of Hong Kong. This finding aligns with the fact that NO_2 directly contributes to PAN production, whereas NO reduces PA radicals, thereby inhibiting PAN formation. Based on the scenario analysis (Empirical Kinetic Modeling Approach (EKMA)), all data points for the 22 days fell above the ridge line (Fig. 8(c)). A reduction

in VOCs at these points resulted in lower PAN concentrations, indicating that PAN formation at IUE was influenced by VOCs and thus VOC-sensitive. Our previous research also found that in this coastal city, PAN generation is limited by VOCs during the spring and autumn seasons. The difference is that previous studies indicated that reducing NO_2, like reducing NO, also leads to an increase in PAN concentration in spring and autumn (Liu et al., 2022a). This is because the NO_x concentration in spring and autumn is significantly higher than in summer, which is consistent with that both NO_2 and NO inhibit the formation of PAN in regions with high NO_x concentrations (Liu et al., 2024).

We divided the RIRs for different species into haze and clean periods and found that the RIRs during clean periods were consistently higher than those during haze periods (Fig. 8(d)), which indicated that altering the concentrations of these species during clean periods had a greater impact on PAN formation. The rapid thermal decomposition of PAN at high temperatures is likely the primary reason. During the haze period, the main source of PA radical was PAN decomposition, which accounted for 68.22 %, and the other sources were smaller than that during the clean period (the source of the PA radical would be demonstrated in the following paragraph). Therefore, the sensitivity of PAN production to precursors and HONO & O_3 producing OH became lower during the haze period (Liu et al., 2021b; Liu et al., 2022a).

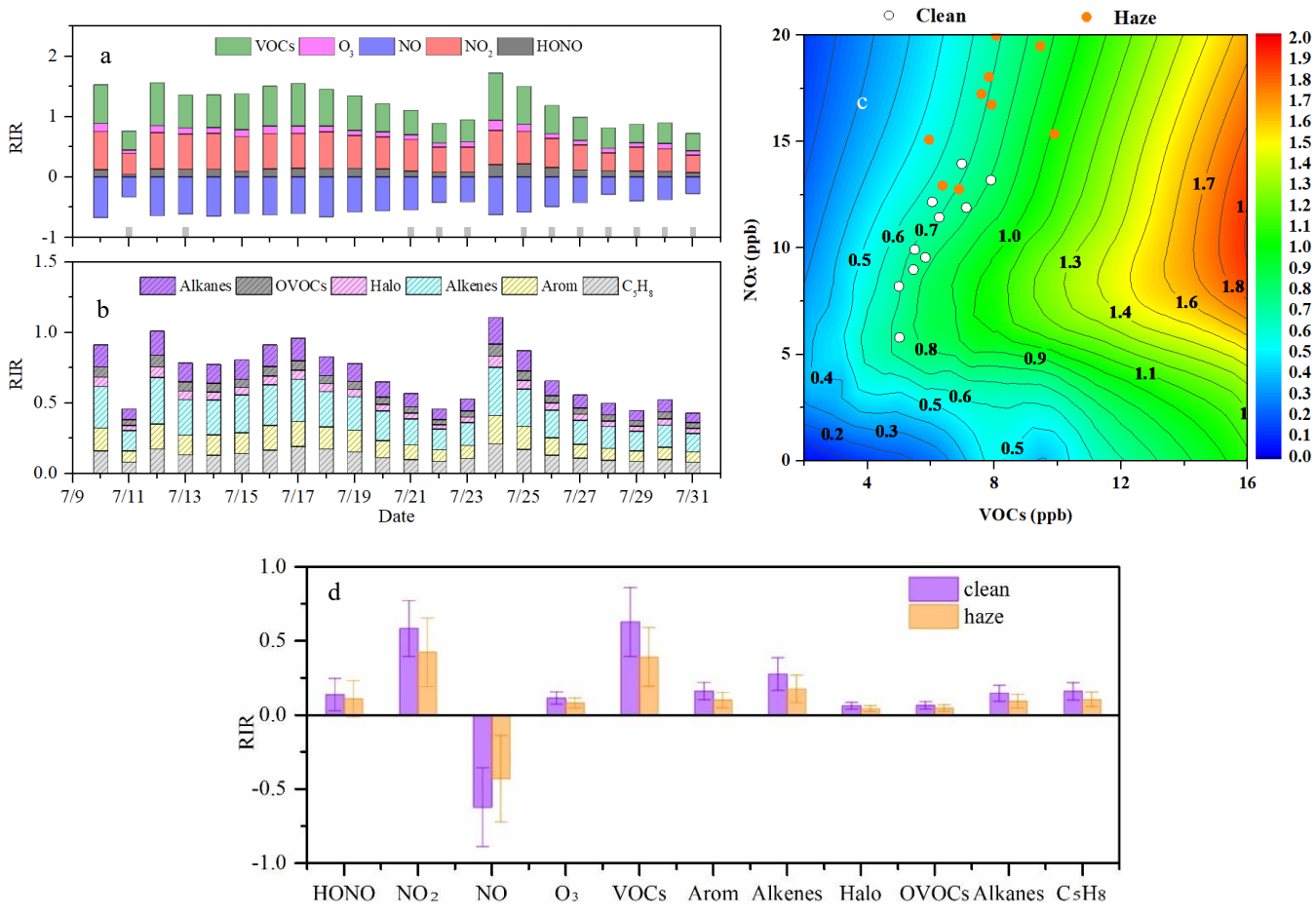

Figure 8. These four figures illustrate the RIR of PAN formation to major precursors (a), the impact of different VOCs species (b), the isopleth diagrams of PAN formation (c), and a comparison of RIRs between clean and polluted periods (d).

As shown in Fig. 9, ΔHO_2 and ΔOH are positive for most periods, accounting for 72.16 % and 70.83 %, respectively, indicating that the PAN mechanism promotes the generation of HO_2 and OH. Over the entire period, ΔHO_2 is $8.43 \cdot 10^{-5}$ ppb, with no significant difference between clean and hazy periods, being $8.18 \cdot 10^{-5}$ ppb and $8.64 \cdot 10^{-5}$ ppb respectively (Table S2). OH behaves similarly, with ΔOH being $4.55 \cdot 10^{-7}$ ppb over the entire period, and also showing no significant difference between clean and hazy periods, being $4.94 \cdot 10^{-7}$ ppb and $4.23 \cdot 10^{-7}$ ppb respectively (Table S2). The increase in simulated OH and HO_2 concentrations suggests that PAN photochemistry is in favor of radical formation and atmospheric oxidative capacity at this site (Liu et al., 2024). Unlike HO_2 and OH, ΔRO_2 and ΔNO_2 are negative for most periods, accounting for 53.22 % and 67.23 %, respectively, because PAN formation uses up PA and NO_2, the reduction in PA leads to a decrease in the amount of RO_2. Over the entire period, ΔRO_2 is $-6.4 \cdot 10^{-4}$ ppb, with no significant difference between clean and hazy periods, being $-6.11 \cdot 10^{-4}$ ppb and $-6.55 \cdot 10^{-4}$ ppb respectively (Table S2). The average value of ΔNO_2 during the entire observation period is -0.17 ppb respectively, with significant differences between hazy and clean periods (Table S2). Specifically, ΔNO_2 is -0.22 during hazy periods and only -0.11 during clean periods, indicating that the PAN mechanism consumes more NO_2 during hazy periods. Although ΔNO is positive for most periods, accounting for 78.79 %, the overall mean is -0.01, with significant differences between hazy and clean periods (Table S2). ΔNO is -0.05 during hazy periods, showing an inhibitory effect, while it is 0.03 during clean periods, showing a promoting effect.

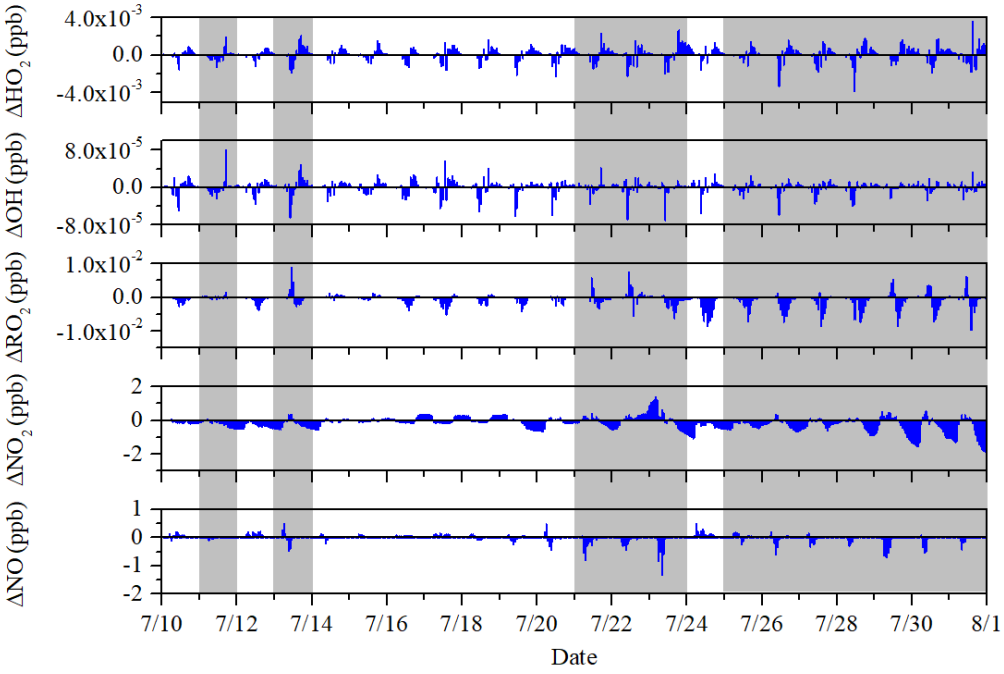

Figure 9. The time series of ΔHO_2, ΔOH, ΔRO_2, ΔNO_2, and ΔNO. The ΔHO_2, ΔOH, ΔRO_2, ΔNO_2, and ΔNO is calculated as the base scenario with the PAN mechanism minus the scenario without the PAN mechanism.

As shown in Fig.10 (a), the PAN mechanism inhibited 85.80 % of net O_3 production during the entire observation period, with inhibition rates (the percentage of negative ΔNet (O_3)) of 83.75 % and 87.50 % during clean and haze periods, respectively. This result is consistent with previous spring observations at the same site, where the inhibition rate was 83 % (Liu et al., 2022a). The

PAN mechanism mainly inhibits the net O_3 generation by increasing the RO_2+NO_2 reaction (Fig.10(a)), with negligible impact from other reactions (Fig. S14). As shown in Fig.10(b), the diurnal variation trend indicates that the PAN mechanism's inhibitory effect on O_3 is significantly greater during haze periods than during clean periods. Additionally, regardless of whether it is during haze periods or clean periods, the PAN mechanism's inhibitory effect on O_3 is significantly greater during the day than at night. These phenomena all indicate that the higher the PAN concentration, the more pronounced the inhibitory effect of the PAN mechanism on O_3 (Fig.10(c)). Under the condition of low precursors (including NO_x and VOCs) conditions, competition among these precursors may limit their secondary transformation, thus resulting in inhibition (Liu et al., 2024).

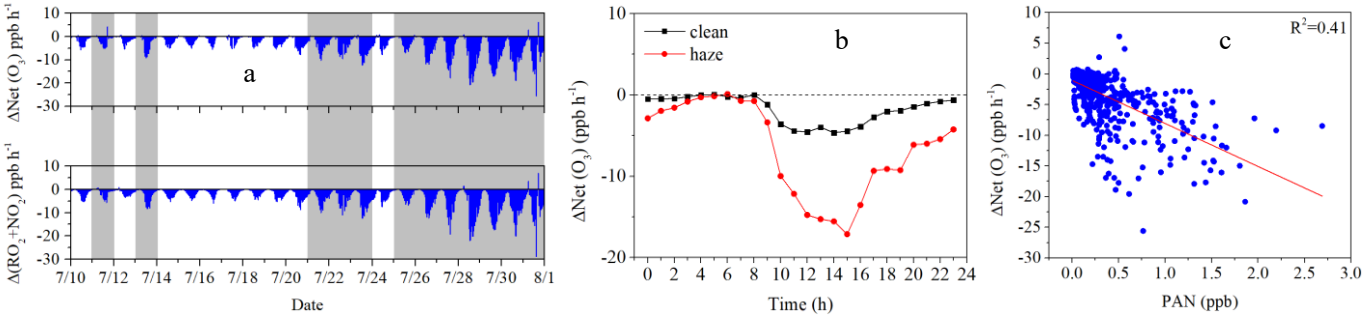

Figure 10. (a) Time series plot of ΔNet (O_3) and the reaction of Δ(RO_2+NO_2), (b) Diurnal variation of ΔNet (O_3) during clean and hazy conditions, (c) Correlation between ΔNet (O_3) and PAN. ΔNet (O_3) and Δ(RO_2+NO_2) are calculated as the base scenario with the PAN mechanism minus the scenario without the PAN mechanism.

Conclusion

This study thoroughly investigated the summertime PAN formation mechanism and established its connection to haze pollution. In addition to NO and TVOCs, the concentration of all pollutants during the haze period is above twice that during the clean period, indicating that the oxidation of NO and TVOCs during the haze period is stronger, which is conducive to the oxidation of NO and TVOCs into secondary pollutants, such as O_3 and PAN. The slopes of linear regression between the daily maximum values of PAN and O_3 were 0.021 ppb ppb^{-1} and 0.009 ppb ppb^{-1} for clean and hazy condition, respectively, implies that PAN precursors accounted for only a small fraction of the total VOCs, especially for hazy condition. High temperature should be another factor contributing to the lower production efficiency of PAN in the southeast coastal region. During the whole observation period, the IOA=0.75, indicating that the MCM model is well-suited for exploring the photochemical formation of PAN. During the clean period, simulation results were better than during the haze period (R^2: 0.68 vs. 0.47, slope K: 0.91 vs. 0.75), indicating that some reactions related to PAN generation or destruction might be missing in the MCM during the hazy period. Additionally, the simulated net production rate of PAN becomes negative with PAN constrained. However, the observed increase in PAN concentrations indicates that the actual net production rate is positive, suggesting that there are additional sources contributing to PAN generation that are not considered in the MCM mechanism. Through XGBoost-SHAP machine learning, and given the significant positive correlation between PAN and NO_3^- (R= 0.37) at the 0.01 level, and their peak around noon, they likely share a common source. Both RIR and

EKMA indicate that PAN formation in this region is VOC-controlled. Controlling emissions of VOCs, particularly alkenes, C_5H_8, and aromatics, would be beneficial for mitigating PAN pollution. The RIR results also show that during the clean period, PAN is more sensitive to changes in various pollutants than during the haze period, highlighting the significant importance of deep emission reductions. PAN presented the promotion effects on OH and HO_2, while inhibited O_3 formation, RO_2, NO and NO_2. This study improves our thorough understanding of PAN photochemistry and offers valuable scientific guidance for the future management of PAN pollution.

Data availability

The observation data at this site are available from the authors upon request.

Authorship Contribution Statement

Baoye Hu: Methodology, Formal analysis, Investigation, Data curation, Writing – original draft. **Naihua Chen**: Software, Formal analysis. **Rui Li:** Software, Formal analysis. **Mingqiang Huang**: Software. **Jinsheng Chen**: Funding acquisition, Supervision, Writing - Review & Editing. **Youwei Hong**: Formal analysis. **Lingling Xu**: Investigation. Xiaolong Fan: Investigation. **Mengren Li**: Investigation. **Lei Tong**: Investigation. **Qiuping Zheng**: Investigation. **Yuxiang Yang:** Writing - Review & Editing

Competing interests

The authors declare that they have no conflict of interest.

Acknowledgments

This work was supported by the National Natural Science Foundation of China (grant nos. 42305102, U22A20578), the guiding project of seizing the commanding heights of “self-purifying city” (NO. IUE-CERAE-202402), Natural Science Foundation of Fujian Province (grant No. 2023J05179), Natural Science Foundation of Zhangzhou City (grant No. ZZ2023J07), the Fund of Minnan Normal University President (grant No. KJ2021009). This study was funded by Xiamen Atmospheric Environment Observation and Research Station of Fujian Province, and Fujian Key Laboratory of Atmospheric Ozone Pollution Prevention (Institute of Urban Environment, Chinese Academy of Sciences).

Supplementary information

Attached please find supplementary information associated with this article.

Reference

Behera, S. N., Sharma, M., Aneja, V. P., and Balasubramanian, R.: Ammonia in the atmosphere: a review on emission sources, atmospheric chemistry and deposition on terrestrial bodies, Environ. Sci. Pollut. Res., 20, 8092-8131, 10.1007/s11356-013-2051-9, 2013.

Cox, R. A., & Roffey, M. J. : Thermal decomposition of peroxyacetylnitrate in the presence of nitric oxide. Environ. Sci. Tech., 11, 900-906, 10.1021/es60132a010, 1977.

Duan, J., Qin, M., Ouyang, B., Fang, W., Li, X., Lu, K., Tang, K., Liang, S., Meng, F., Hu, Z., Xie, P., Liu, W., and Häseler, R.: Development of an incoherent broadband cavity-enhanced absorption spectrometer for in situ measurements of HONO and NO_2, Atmos. Meas. Tech., 11, 4531-4543, 10.5194/amt-11-4531-2018, 2018.

Hong, Z., Li, M., Wang, H., Xu, L., Hong, Y., Chen, J., Chen, J., Zhang, H., Zhang, Y., Wu, X., Hu, B., and Li, M.: Characteristics of atmospheric volatile organic compounds (VOCs) at a mountainous forest site and two urban sites in the southeast of China, Sci. Total Environ., 657, 1491-1500, 10.1016/j.scitotenv.2018.12.132, 2019.

Hu, B., Liu, T., Hong, Y., Xu, L., Li, M., Wu, X., Wang, H., Chen, J., and Chen, J.: Characteristics of peroxyacetyl nitrate (PAN) in a coastal city of southeastern China: Photochemical mechanism and pollution process, Sci. Total Environ., 719, 10.1016/j.scitotenv.2020.137493, 2020.

Hu, B., Wang, Y., Chen, J., Chen, N., Hong, Y., Xu, L., Fan, X., Li, M., and Tong, L.: The observation of atmospheric HONO by wet-rotating-denuder ion chromatograph in a coastal city: Performance and influencing factors, Environ. Pollut., 356, 10.1016/j.envpol.2024.124355, 2024.

Hu, B., Duan, J., Hong, Y., Xu, L., Li, M., Bian, Y., Qin, M., Fang, W., Xie, P., and Chen, J.: Exploration of the atmospheric chemistry of nitrous acid in a coastal city of southeastern China: results from measurements across four seasons, Atmos. Chem. Phys., 22, 371-393, 10.5194/acp-22-371-2022, 2022.

Li, H., Yang, Y., Su, H., Wang, H., Wang, P., and Liao, H.: Ozone pollution in China affected by climate change in a carbon neutral future as predicted by a process-based interpretable machine learning method, Geophys. Res. Lett., 51, 10.1029/2024gl109520, 2024.

Lin, Z., Xu, L., Yang, C., Chen, G., Ji, X., Li, L., Zhang, K., Hong, Y., Li, M., Fan, X., Hu, B., Zhang, F., and Chen, J.: Trends of peroxyacetyl nitrate and its impact on ozone over 2018–2022 in urban atmosphere, Npj Clim. Atmos. Sci, 7, 10.1038/s41612-024-00746-7, 2024.

Liu, L., Wang, X., Chen, J., Xue, L., Wang, W., Wen, L., Li, D., and Chen, T.: Understanding unusually high levels of peroxyacetyl nitrate (PAN) in winter in Urban Jinan, China, J. Environ. Sci., 71, 249-260, 10.1016/j.jes.2018.05.015, 2018.

Liu, T., Chen, G., Chen, J., Xu, L., Li, M., Hong, Y., Chen, Y., Ji, X., Yang, C., Chen, Y., Huang, W., Huang, Q., and Wang, H.: Seasonal characteristics of atmospheric peroxyacetyl nitrate (PAN) in a coastal city of Southeast China: Explanatory factors

and photochemical effects, Atmos. Chem. Phys., 22, 4339-4353, 10.5194/acp-22-4339-2022, 2022a.

Liu, T., Hong, Y., Li, M., Xu, L., Chen, J., Bian, Y., Yang, C., Dan, Y., Zhang, Y., Xue, L., Zhao, M., Huang, Z., and Wang, H.: Atmospheric oxidation capacity and ozone pollution mechanism in a coastal city of southeastern China: analysis of a typical photochemical episode by an observation-based model, Atmos. Chem. Phys., 22, 2173-2190, 10.5194/acp-22-2173-2022, 2022b.

Liu, T., Wang, Y., Cai, H., Wang, H., Zhang, C., Chen, J., Dai, Y., Zhao, W., Li, J., Gong, D., Chen, D., Zhai, Y., Zhou, Y., Liao, T., and Wang, B.: Complexities of peroxyacetyl nitrate photochemistry and its control strategies in contrasting environments in the Pearl River Delta region, Npj Clim. Atmos. Sci, 7, 10.1038/s41612-024-00669-3, 2024.

Liu, X., Guo, H., Zeng, L., Lyu, X., Wang, Y., Zeren, Y., Yang, J., Zhang, L., Zhao, S., Li, J., and Zhang, G.: Photochemical ozone pollution in five Chinese megacities in summer 2018, Sci. Total Environ., 801, 149603, 10.1016/j.scitotenv.2021.149603, 2021a.

Liu, Y., Shen, H., Mu, J., Li, H., Chen, T., Yang, J., Jiang, Y., Zhu, Y., Meng, H., Dong, C., Wang, W., and Xue, L.: Formation of peroxyacetyl nitrate (PAN) and its impact on ozone production in the coastal atmosphere of Qingdao, North China, Sci. Total Environ., 778, 10.1016/j.scitotenv.2021.146265, 2021b.

Lu, X., Zhang, L., Wang, X., Gao, M., Li, K., Zhang, Y., Yue, X., and Zhang, Y.: Rapid Increases in Warm-Season Surface Ozone and Resulting Health Impact in China Since 2013, Environ. Sci. Tech. Lett., 7, 240-247, 10.1021/acs.estlett.0c00171, 2020.

Marley, N. A., Gaffney, J. S., Ramos-Villegas, R., and ´, B. C. G.: Comparison of measurements of peroxyacyl nitrates and primary carbonaceous aerosol concentrations in Mexico City determined in 1997 and 2003, Atmos. Chem. Phys., 7, 2277-2285, 2007a.

Marley, N. A., Gaffney, J. S., Ramos-Villegas, R., and Gonzalez, B. C.: Comparison of measurements of peroxyacyl nitrates and primary carbonaceous aerosol concentrations in Mexico City determined in 1997 and 2003, Atmos. Chem. Phys., 7, 2277–2285, 2007b.

Pratap, V., Carlton, A. G., Christiansen, A. E., and Hennigan, C. J.: Partitioning of ambient organic gases to inorganic salt solutions: influence of salt identity, ionic strength, and pH, Geophys. Res. Lett., 48, 10.1029/2021gl095247, 2021.

Roberts, J. M., Flocke, F., Stroud, C. A., Hereid, D., Williams, E., Fehsenfeld, F., Brune, W., Martinez, M., and Harder, H.: Ground-based measurements of peroxycarboxylic nitric anhydrides (PANs) during the 1999 Southern Oxidants Study Nashville Intensive, J Geophys Res-Atmos, 107, ACH 1-1-ACH 1-10, 10.1029/2001jd000947, 2002.

Senum, G. I., Fajer, R., & Gaffney, J. S. Fourier transform infrared spectroscopic study of the thermal stability of peroxyacetyl nitrate, J. Phys. Chem., 90, 152-156, 10.1021/j100273a034, 1986.

Sun, M., Cui, J. n., Zhao, X., and Zhang, J.: Impacts of precursors on peroxyacetyl nitrate (PAN) and relative formation of PAN to ozone in a southwestern megacity of China, Atmos. Environ., 231, 10.1016/j.atmosenv.2020.117542, 2020.

Sun, M., Zhou, Y., Wang, Y., Qiao, X., Wang, J., and Zhang, J.: Heterogeneous reaction of peroxyacetyl nitrate on real-world $PM_{2.5}$

aerosols: Kinetics, influencing Factors, and atmospheric implications, Environ. Sci. Tech., 56, 9325-9334, 10.1021/acs.est.2c03050, 2022.

Taylor, O. C.: Importance of peroxyacetyl nitrate (PAN) as a phytotoxic air pollutant, J. Air Pollut. Control Assoc., 19, 347-351, 10.1080/00022470.1969.10466498, 1969.

Tuazon, E. C., Carter, W. P., & Atkinson, R. : Thermal decomposition of peroxyacetyl nitrate and reactions of acetyl peroxy radicals with nitric oxide and nitrogen dioxide over the temperature range 283-313 K. J. Phys. Chem., 95, 2434-2437, 10.1021/j100159a059, 1991.

Wang, B., Shao, M., Roberts, J. M., Yang, G., Yang, F., Hu, M., Zeng, L., Zhang, Y., and Zhang, J.: Ground-based on-line measurements of peroxyacetyl nitrate (PAN) and peroxypropionyl nitrate (PPN) in the Pearl River Delta, China. , Int. J. Environ. Anal. Chem., 90, 548−559, 10.1080/03067310903194972, 2010.

Wang, H., Lyu, X., Guo, H., Wang, Y., Zou, S., Ling, Z., Wang, X., Jiang, F., Zeren, Y., Pan, W., Huang, X., and Shen, J.: Ozone pollution around a coastal region of South China Sea: interaction between marine and continental air, Atmos. Chem. Phys., 18, 4277-4295, 10.5194/acp-18-4277-2018, 2018.

Wang, Y., Liu, T., Gong, D., Wang, H., Guo, H., Liao, M., Deng, S., Cai, H., and Wang, B.: Anthropogenic pollutants induce changes in peroxyacetyl nitrate formation intensity and pathways in a mountainous background atmosphere in southern China, Environ. Sci. Tech., 10.1021/acs.est.2c02845, 2023.

Wu, X., Xu, L., Hong, Y., Chen, J., Qiu, Y., Hu, B., Hong, Z., Zhang, Y., Liu, T., Chen, Y., Bian, Y., Zhao, G., Chen, J., and Li, M.: The air pollution governed by subtropical high in a coastal city in Southeast China: Formation processes and influencing mechanisms, Sci. Total Environ., 692, 1135-1145, 10.1016/j.scitotenv.2019.07.341, 2019.

Xu, W., Zhang, G., Wang, Y., Tong, S., Zhang, W., Ma, Z., Lin, W., Kuang, Y., Yin, L., and Xu, X.: Aerosol promotes peroxyacetyl nitrate formation during winter in the North China Plain, Environ. Sci. Technol., 55, 3568-3581, 10.1021/acs.est.0c08157, 2021.

Xu, X., Zhang, H., Lin, W., Wang, Y., Xu, W., and Jia, S.: First simultaneous measurements of peroxyacetyl nitrate (PAN) and ozone at Nam Co in the central Tibetan Plateau: impacts from the PBL evolution and transport processes, Atmos. Chem. Phys., 18, 5199-5217, 10.5194/acp-18-5199-2018, 2018.

Xu, Z., Xue, L., Wang, T., Xia, T., Gao, Y., Louie, P. K. K., and Luk, C. W. Y.: Measurements of peroxyacetyl nitrate at a background site in the Pearl River Delta region: production efficiency and regional transport, Aerosol Air Qual. Res., 15, 833-841, 10.4209/aaqr.2014.11.0275, 2015.

Xue, L., Wang, T., Wang, X., Blake, D. R., Gao, J., Nie, W., Gao, R., Gao, X., Xu, Z., Ding, A., Huang, Y., Lee, S., Chen, Y., Wang, S., Chai, F., Zhang, Q., and Wang, W.: On the use of an explicit chemical mechanism to dissect peroxy acetyl nitrate formation, Environ. Pollut., 195, 39-47, 10.1016/j.envpol.2014.08.005, 2014.

Xue, L. K., Wang, T., Guo, H., Blake, D. R., Tang, J., and Zhang, X. C.: Sources and photochemistry of volatile organic compounds

in the remote atmosphere of western China: results from the Mt. Waliguan Observator, Atmos. Chem. Phys., 13, 8551-8567, 10.5194/acp-13-8551-2013, 2013.

Yang, X., Wu, K., Wang, H., Liu, Y., Gu, S., Lu, Y., Zhang, X., Hu, Y., Ou, Y., Wang, S., and Wang, Z.: Summertime ozone pollution in Sichuan Basin, China: Meteorological conditions, sources and process analysis, Atmos. Environ., 226, 10.1016/j.atmosenv.2020.117392, 2020.

Ye, C., Zhang, N., Gao, H., and Zhou, X.: Photolysis of particulate nitrate as a source of HONO and NO_x, Environ. Sci. Technol., 51, 6849-6856, 10.1021/acs.est.7b00387, 2017.

Yuan, J., Ling, Z., Wang, Z., Lu, X., Fan, S., He, Z., Guo, H., Wang, X., and Wang, N.: PAN–precursor relationship and process analysis of PAN variations in the Pearl River Delta region, Atmos., 9, 10.3390/atmos9100372, 2018.

Yukihiro, M., Hiramatsu, T., Bouteau, F., Kadono, T., and Kawano, T.: Peroxyacetyl nitrate-induced oxidative and calcium signaling events leading to cell death in ozone-sensitive tobacco cell-line, Plant Signal Behav., 7, 113-120, 10.4161/psb.7.1.18376, 2012.

Zeng, L., Fan, G. J., Lyu, X., Guo, H., Wang, J. L., and Yao, D.: Atmospheric fate of peroxyacetyl nitrate in suburban Hong Kong and its impact on local ozone pollution, Environ. Pollut., 252, 1910-1919, 10.1016/j.envpol.2019.06.004, 2019.

Zhai, S., Jacob, D. J., Franco, B., Clarisse, L., Coheur, P., Shah, V., Bates, K. H., Lin, H., Dang, R., Sulprizio, M. P., Huey, L. G., Moore, F. L., Jaffe, D. A., and Liao, H.: Transpacific transport of Asian peroxyacetyl nitrate (PAN) observed from satellite: implications for ozone, Environ. Sci. Tech., 58, 9760-9769, 10.1021/acs.est.4c01980, 2024.

Zhang, G., Mu, Y., Zhou, L., Zhang, C., Zhang, Y., Liu, J., Fang, S., and Yao, B.: Summertime distributions of peroxyacetyl nitrate (PAN) and peroxypropionyl nitrate (PPN) in Beijing: Understanding the sources and major sink of PAN, Atmos. Environ., 103, 289−296, 10.1016/j.atmosenv.2014.12.035, 2015.

Zhang, J., Guo, Y., Qu, Y., Chen, Y., Yu, R., Xue, C., Yang, R., Zhang, Q., Liu, X., Mu, Y., Wang, J., Ye, C., Zhao, H., Sun, Q., Wang, Z., and An, J.: Effect of potential HONO sources on peroxyacetyl nitrate (PAN) formation in eastern China in winter, J. Environ. Sci. (China), 94, 81-87, 10.1016/j.jes.2020.03.039, 2020.

Zhang, J. M., Wang, T., Ding, A. J., Zhou, X. H., Xue, L. K., Poon, C. N., Wu, W. S., Gao, J., Zuo, H. C., Chen, J. M., Zhang, X. C., and Fan, S. J.: Continuous measurement of peroxyacetyl nitrate (PAN) in suburban and remote areas of western China, Atmos. Environ., 43, 228-237, 10.1016/j.atmosenv.2008.09.070, 2009.

Zhu, J., Wang, S., Wang, H., Jing, S., Lou, S., Saiz-Lopez, A., and Zhou, B.: Observationally constrained modeling of atmospheric oxidation capacity and photochemical reactivity in Shanghai, China, Atmos. Chem. Phys., 20, 1217-1232, 10.5194/acp-20-1217-2020, 2020.